

Effectively Transparent Front Contacts for Optoelectronic Devices

Rebecca Saive, Aleca M. Borsuk, Hal S. Emmer, Colton R. Bukowsky, John V. Lloyd, Sisir Yalamanchili, and Harry A. Atwater*

Optoelectronic devices such as light emitting diodes, photodiodes, and solar cells play an important and expanding role in modern technology. Photovoltaics is one of the largest optoelectronic industry sectors and an ever-increasing component of the world's rapidly growing renewable carbon-free electricity generation infrastructure. In recent years, the photovoltaics field has dramatically expanded owing to the large-scale manufacture of inexpensive crystalline Si and thin film cells and modules. The current record efficiency ($\eta = 25.6\%$) Si solar cell utilizes a heterostructure intrinsic thin layer (HIT) design^[1] to enable increased open circuit voltage, while more mass-manufacturable solar cell architectures feature front contacts.^[2,3] Thus improved solar cell front contact designs are important for future large-scale photovoltaics with even higher efficiency.

Improving the state of the art for optoelectronic device technology requires optimal photon management. For example, in conventional solar cells or photodiodes with front and rear contacts, a nonnegligible fraction of the incoming solar power is immediately lost at the front contact either through absorption, as in the case of transparent conductive oxides or through reflection at contact grid fingers. As a result, many groups have recently proposed design schemes to mitigate front contact losses, such as less absorbing transparent conductive oxides,^[4–8] or less reflective metal contacts such as nanowire grids,^[9,10] fractal contacts,^[11] contacts with different shapes,^[12–16] and various other approaches.^[17–21] Very high contact transparency usually comes at the expense of reduced conductivity, which in turn leads to series resistance and device electrical losses. A comparison of the photonic designs for different recently developed contacts is shown in Section S3 (Supporting Information).

For any flat plate solar cell, the front contact design process involves a balance of the grid finger resistance, grid finger

shadow loss, and the sheet resistance and absorption losses associated with planar layers that facilitate lateral carrier transport to the grid fingers.^[22,23] For high efficiency silicon heterojunction (HIT) solar cells, contact design requires a trade-off between grid finger resistance and the sheet resistance and transmission losses of the transparent conducting oxide (TCO)/amorphous silicon structures coating the cell front surface.^[24]

In this paper, we describe a new front contact design principle that overcomes both shadowing losses and parasitic absorption without reducing the conductivity. By redirecting the scattered light incident on the front contact to the solar cell active absorber layer surface, micrometer-scale triangular cross-section grid fingers can perform as effectively transparent and highly conductive front contacts. Previously, researchers have designed light harvesting strings that serve to obliquely reflect light, which is then redirected into the cell by total internal reflection from the encapsulation layers.^[16] By contrast our front contact design does not require total internal reflection at the encapsulation layer. Furthermore in our design, the contact fingers are micrometer sized and can be placed very close together such that a TCO with reduced thickness can be used—and in some cases the TCO layer might possibly be omitted completely. We demonstrate with simulations and experimental results that designs utilizing effectively transparent triangular cross-section grid fingers rather than conventional front contacts have the potential to provide 99.86% optical transparency while ensuring efficient lateral transport corresponding to a sheet resistance of $4.8 \Omega \text{ sq}^{-1}$ due to their close spacing of only $40 \mu\text{m}$. Thus effectively transparent contacts have potential as replacements for both the front grid and TCO layer used, e.g., in HIT solar cells. While related schemes for contacts were envisioned early in the development of photovoltaics technology,^[25] they have not found application in current photovoltaic technology, which is increasingly dominated by high efficiency silicon photovoltaics. Moreover, the effectively transparent front contact design is conceptually quite general and applicable to almost any other front-contacted solar cell or optoelectronic device. For example, we obtained similar experimental results when applying our structures to InGaP-based solar cells.

Figure 1a,b shows the steady-state electric field magnitude distribution of a freestanding triangular contact and a flat contact, respectively, with 550 nm monochromatic plane wave illumination normally incident at the top of the simulation cell. For planar grid fingers, part of the incident light is reflected back toward the incidence direction, as is apparent from the high electric field density above the contact plane. By contrast, the triangular cross-section grid finger does not exhibit a similar back reflection, as indicated by the lack of an increased electric

Dr. R. Saive, A. M. Borsuk, Dr. H. S. Emmer,
C. R. Bukowsky, J. V. Lloyd, S. Yalamanchili,
Prof. H. A. Atwater
Department of Applied Physics
and Materials Science
California Institute of Technology
Pasadena, CA 91125, USA
E-mail: haa@caltech.edu



This is an open access article under the terms of the Creative Commons Attribution-NonCommercial License, which permits use, distribution and reproduction in any medium, provided the original work is properly cited and is not used for commercial purposes.

The copyright line of this paper was changed 1 August 2016 after initial publication.

DOI: 10.1002/adom.201600252

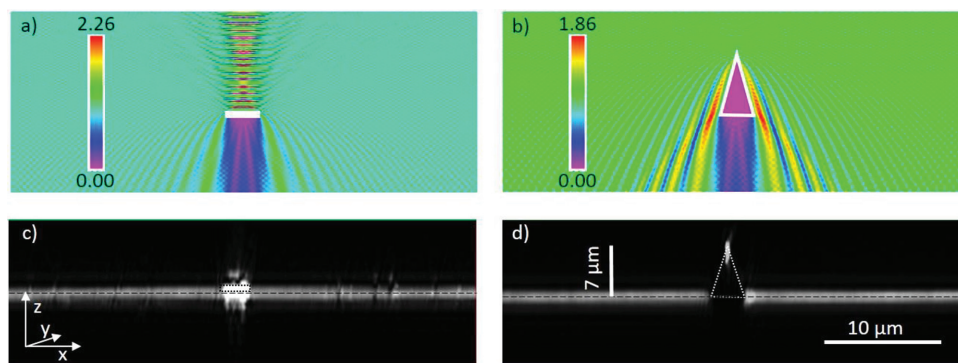


Figure 1. Simulated steady-state electric field magnitude distribution at 550 nm incident light for a free-standing a) flat contact and b) triangular cross-section contact. Cross-sectional profiles from 3D confocal scanning microscope image of c) flat contact and d) triangular cross-section contact.

field density in the incidence direction. However an enhancement of the electric field is seen in the forward scattering direction, behind the contact, explaining its effective transparency.

Figure 1c,d is cross-sections from 3D confocal scanning microscopy measurements of a flat grid line grid finger and triangular cross-section grid finger, respectively, on a Si heterojunction solar cell. The focused confocal illumination laser was scanned in x -, y -, and z -direction and the displayed images show a cross-section of the signal at constant y -value. A dashed black line in each image marks the solar cell surface. In Figure 1c it can be seen that in the vicinity of the flat contact (dashed black rectangle), the reflection signal is much stronger than at the antireflection-coated solar cell surface. In Figure 1d the position of the triangular grid finger is marked by a dashed white triangle. Along the contact sidewalls, it appears black suggesting that there is no reflection back to the incident light source from the sidewalls. Only the tip shows some reflec-

tion, which can be attributed to finite radius of curvature of the tip, as confirmed by optical simulations. Simulations and experiments indicate that triangular cross-section grid fingers outperform flat grid fingers between 0° and 55° incident angle in a plane perpendicular to the grid finger length. The performance of the triangular cross-section grid fingers is not altered if the incident angle of the light is varied in a plane parallel to the contact lines. Triangular grid fingers show superior performance for wavelengths between 250 and 1400 nm. Simulations and experiments supporting these conclusions can be found in the Section S1 (Supporting Information). In the simulations as well as in the experiments, the grid fingers were $2.5 \mu\text{m}$ wide and the triangular cross-section grid fingers were $7.0 \mu\text{m}$ high. The period of the pattern was $40 \mu\text{m}$.

Figure 2 shows spatially resolved measurements of reflection (a and b) and the photocurrent (c and d) of an area spanned by flat grid fingers (a and c) and by triangular cross-section grid

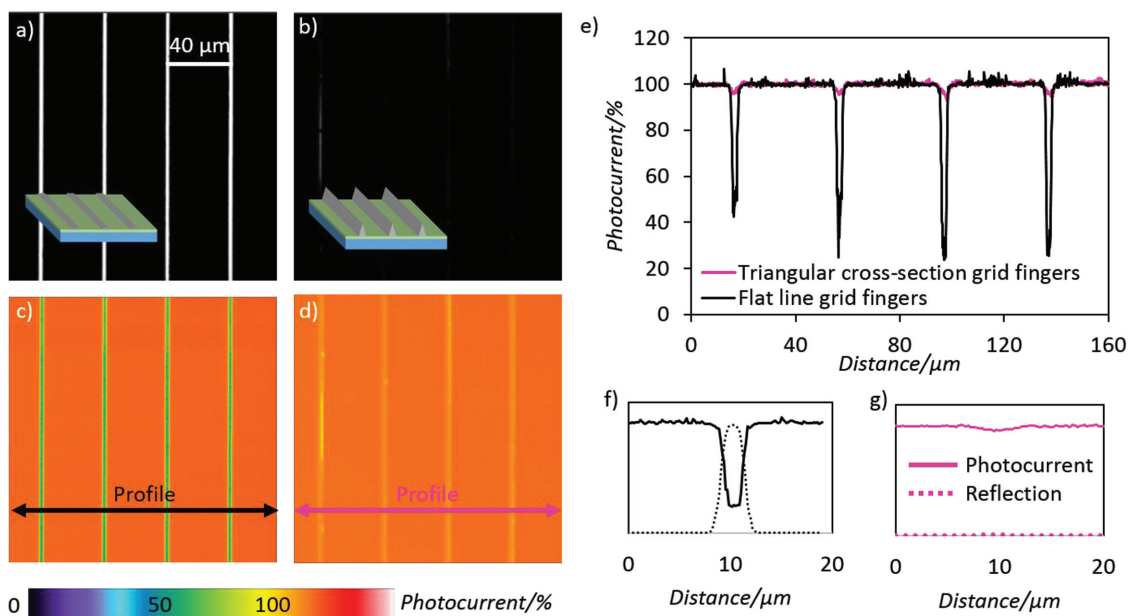


Figure 2. Spatially resolved reflection of a) flat lines and b) effectively transparent triangular cross-section contacts and the corresponding spatially resolved photocurrent for c) flat lines and d) effectively transparent triangular cross-section contacts determined by laser beam induced photocurrent measurements at a wavelength of 543 nm. e) Line-scan profiles of the photocurrent taken across flat contact lines and across lines with triangular cross-section. Photocurrent and reflection profiles taken over one f) flat and g) triangular cross-section line.

fingers (b and d) on the same solar cell. In Figure 2a, the dark regions correspond to the antireflection-coated cell substrate while the bright regions correspond to flat silver contacts. In Figure 2b, lines with triangular cross-section are aligned with and cover the silver grid fingers in a different area on the same cell. It can be seen that the triangular cross-section grid fingers appear much darker than the flat line grid fingers, in some regions exhibiting no measurable reflection. This has direct influence on the measured photocurrent. As can be seen in Figure 2c, the orange color represents the photocurrent measured in the areas between grid fingers, while the green color corresponds to the grid fingers, illustrating that there is very little photocurrent generated at the position of the flat contact lines.

Figure 2d illustrates the photocurrent in the vicinity of the triangular cross-section grid fingers. The photocurrent at the position of the triangular cross-section grid fingers is relatively higher as seen by the yellow color, while the photocurrent between grid fingers is the same as in Figure 2b. The difference in photocurrent collection near the grid fingers becomes very apparent when comparing line-scan profiles of the photocurrent taken across flat grid fingers and across grid fingers with triangular cross-section, as shown in Figure 2e. Figure 2f,g shows higher resolution profiles, plotted with similar y-axis scales, over one flat and one triangular cross-section line, respectively. We note that in light beam induced current (LBIC) measurements, the position of the laser light is detected rather than the actual location of the current generation. Thus a photocurrent enhancement is visible at the position of the triangular cross-section grid finger although the current is generated next to the grid finger.

Averaging generation photocurrent density over the area shown in Figure 2c indicates a grid finger transparency of 96.67% normalized to the open regions between fingers. This value is higher than one would expect from the areal surface coverage ($\approx 6\%$) since the 100 nm Ag thin film grid fingers are thin enough to be partially transmitting (as can be seen by the nonzero photocurrent signal at the position of the flat lines). (Compare Section S4, Supporting Information) Averaging over the area in Figure 2d indicates a grid finger transparency of 99.74% while the most transparent regions within this area even reach 99.86% contact transparency. The fabrication process was repeated numerous times, and other fabricated samples were found to exhibit slightly lower transparency, but always well above 99%.

Calculations for an indium tin oxide (ITO)-free HIT solar cell featuring closely spaced triangular cross-section grid fingers

with 40 μm period predict a series resistance in lateral transport of $\approx 1.0 \Omega \text{ cm}^2$ (Section S5,^[26] Supporting Information). This, for example, implies the possibility of a HIT cell fabrication process without any ITO layer needed. For other types of solar cells with higher sheet resistance, the grid fingers can in principle be spaced even closer together without deteriorating the transparency (Section S2, Supporting Information). The 40 μm period grid fingers provide measured conductivity that is similar to a homogeneous material^[10] with a sheet resistance of $4.8 \Omega \text{ sq}^{-1}$.

Prototype triangular cross-section grid fingers were fabricated using 3D writing by two-photon lithography (scanning electron microscope (SEM) image shown in Figure 3a), and these prototypes were used as master samples for a gravure printing process (see the Experimental Section). An example of a structure printed with silica sol-gel is shown in Figure 3b

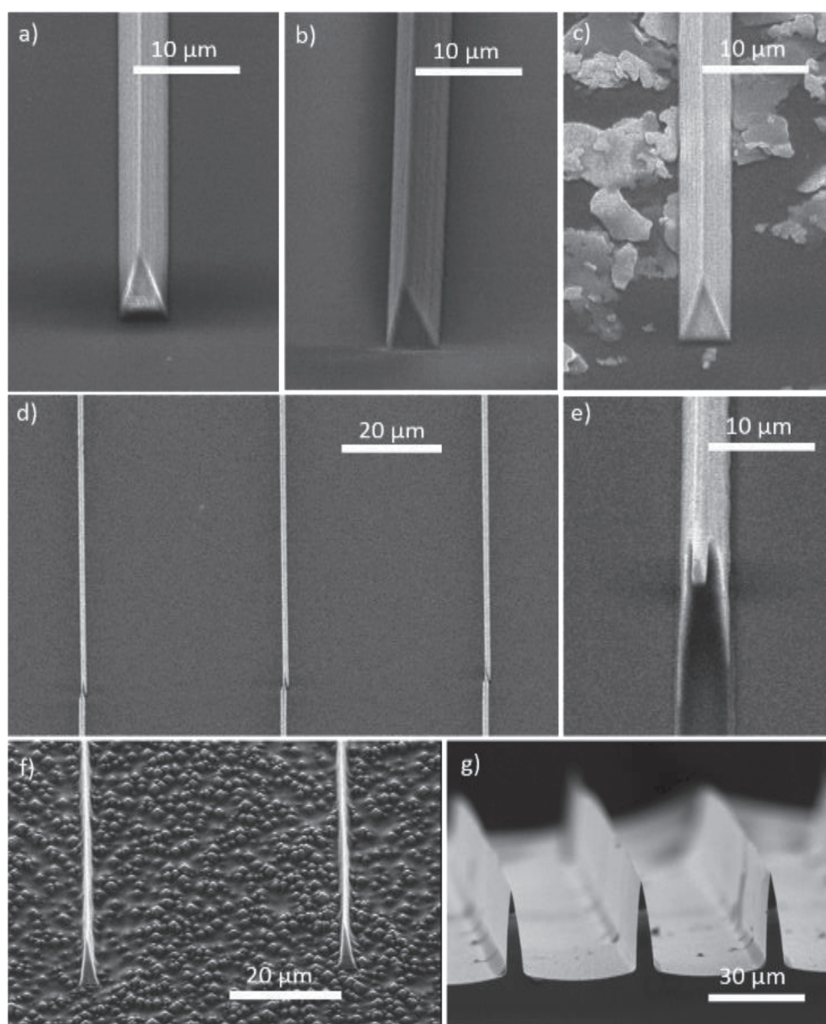


Figure 3. Scanning electron microscope images of a) a triangle structure, prepared by two-photon lithography, that acted as a master for the stamp used to print the triangular cross-section structures shown in (b) and (c). Replicas were printed with b) silica sol-gel and c) silver paste. Panels (d) and (e) illustrate conducting triangular cross-section lines formed via an ink capillary flow process; f) Sol-gel replica formed on a commercial texture-etched silicon solar cell. g) Master sample formation via triangular cross-section structure directly etched into silicon. Images (a)–(f) are taken under a 45° angle, (g) was taken under a 90° angle.

and a silver paste replica is shown in Figure 3c. In both cases even the sidewall texture was reproduced. We have successfully printed over areas up to 8 mm × 8 mm using this technique. If printing is performed with a conductive ink, the printed structures could be used for current transport throughout the whole triangular cross-sectional conductor, leading to very low sheet resistance. However, silver residues on the substrate as can be seen in Figure 3c pose a challenge to this proposition. We were able to overcome this issue by use of a modified stamping process in which the stamp is first applied to the substrate and then loaded with silver ink via a capillary flow process (see method section). Using this procedure, we obtained residue-free triangular grid fingers composed of conductive ink, as seen in Figure 3d,e. Figure 3f illustrates that contact printing can be performed on a textured solar cell front surface; a replica printed on a structured silicon substrate illustrates the potential for implementation on cell surfaces similar to those used in silicon solar cell manufacturing.

Another approach to triangular cross-section grid finger master fabrication is via directional dry etching. The SEM image in Figure 2g illustrates the high aspect ratio lines with triangular cross-section formed by direct etching into silicon. These high aspect ratio silicon structures could be candidates for large-area master stamps for a large-scale gravure printing process for effectively transparent contacts.

We have demonstrated a design for effectively transparent, highly conductive front contacts for optoelectronic devices. Our design is applicable to many types of devices, including, e.g., texture-etched silicon solar cells. Spatially resolved photocurrent measurements at normal incidence show transparency of up to 99.86% in prototype structures, which exhibited a low sheet resistance of 4.8 Ω sq⁻¹. We have also demonstrated a first feasibility step toward large-scale fabrication by gravure printing of contacts using conductive inks.

Experimental Section

The contact design process began with optical simulations that were performed by 2D rigorous coupled wave analysis simulations using RSoft DiffractMOD software. Fabrication of heterojunction with intrinsic thin layer (HIT) solar cells has been detailed in ref. [27]. For our measurements, contacts to HIT cells were fabricated with only 18 nm thin ITO layer to ensure high optical transmission while providing good electrical contact to amorphous silicon. Note that this layer can be thinned or removed if ohmic contact to the top layer is provided.

Prototype samples were prepared by first lithographically defining a flat aluminum finger grid with 2.5 μm width and 40 μm period on planar HIT solar cells. An antireflection coating of 50 nm TiO₂ and 100 nm SiO₂ was deposited on top by electron beam evaporation. 3D two-photon lithography was then used to prepare triangular shaped grid fingers with 2.5 μm width and 7 μm height. We used a Nanoscribe Photonic Professional GT which operates at a wavelength of 780 nm and the photoresist IP-Dip (by Nanoscribe). The writing was performed in piezo mode leading to a voxel width of around 215 nm. A scanning electron microscope image of such a structure is shown in Figure 3a. The triangular shaped lines were coated with silver by evaporation under an angle such that only the sidewalls of triangular shaped grid fingers became metalized, while the active cell surface remained free of metal. Measurements presented in this paper were performed on these prototype structures. Note, that even without metalization a transparency of 99% was achieved. In this configuration, the flat

finger grid geometry determines the sheet resistance. Calculating the equivalent sheet resistance^[10] for the geometry of the fabricated samples (silver lines with 2.5 μm width, 100 nm thickness, and 40 μm distance) leads to 2.6 Ω sq⁻¹ along the direction of the fingers. The experimental sheet resistance was determined from four-point measurements of grids with known geometry that were contacted using bus bars on opposite sides of the grids. We measured a higher value (4.8 Ω sq⁻¹), as our fabricated lines were not perfectly homogeneous and uniform in width. In general, the equivalent sheet resistance value can be straightforwardly modified by altering thickness, width, and distance of the contact lines.

Triangular cross-section structures prepared by two-photon lithography were used as master samples to prepare stamps for a gravure contact printing process (e.g., ref. [28]). Stamps were filled with a silica sol-gel or a silver paste and triangular shaped grid fingers were stamped onto a substrate. An example of a structure printed with silica sol-gel is shown in Figure 3b, a silver paste replica is shown in Figure 3c. In both cases even the sidewall texture was reproduced. To date, we have printed areas up to 8 mm × 8 mm using this technique, and larger areas are possible. When printing is performed using a conductive silver paste, the printed structures could be used for current transport throughout the whole triangular cross-sectional conductor, leading to very low sheet resistance. However, as can be seen in Figure 3c a conventional imprint process leaves unwanted silver residues on the substrate. We developed a method in which the stamp is applied to the sample and is then infilled from a cut side via capillary flow. This results in residue-free printed metal lines shown in Figure 3d,e. The defects seen in the lines at the bottom of Figure 3d are perfect reproductions of the (defective) master stamp and resulted from stitching errors during the two-photon lithography writing process. To date, we have demonstrated ink permeation into stamps over distances of ≈5 mm via ink capillary flow into the stamp. Because commercially produced silicon solar cells commonly feature texture-etched front surfaces to enable light trapping and antireflection, it is important to establish that our process is compatible with such cells. Figure 3f illustrates replication of effectively transparent contacts printed on a commercial texture-etched silicon solar cell. While effectively transparent contact fabrication via two-photon lithography is currently limited to areas of ≈1 cm², we envision that a future gravure printing process using master patterns fabricating by the silicon dry etching method described above will enable stamp and contact fabrication to be scaled to sizes comparable to contemporary silicon solar cells (e.g., 156 cm²).

Triangular shaped lines were furthermore defined by direct etching into silicon. The result is shown in the electron microscope image in Figure 3g. Dry etching of silicon is a possible route to fabrication of large-area master samples for stamp formation. First, an etch mask composed of Al₂O₃ was defined by lithography. Then cryogenic inductively coupled plasma reactive ion etching was performed using SF₆ as etching gas and O₂ as passivation gas. The aspect ratio and taper of the triangular shaped lines etched into the silicon sample can be adjusted by varying the SF₆/O₂ ratio in the plasma (for further details see refs. [29] and [30]). Here we started with a line pattern with ≈2.5 μm width and the etching was performed at 900 W inductively coupled plasma, 5 W capacitive coupled plasma, 70 sccm SF₆, and 9 sccm O₂ for 10 min at -120 °C.

LBIC measurements were performed with a confocal scanning microscope using a 543 nm wavelength laser source. Spatially resolved reflection and photocurrent were simultaneously obtained using an objective with ten times magnification and 0.25 numerical aperture (NA) resulting in a laser spot size of less than 500 nm. For the 3D measurements shown in Figure 2c,d an objective with 20 times magnification and 0.6 NA was used.

Supporting Information

Supporting Information is available from the Wiley Online Library or from the author.

Acknowledgements

The information, data, or work presented herein was funded in part by the U.S. Department of Energy, Energy Efficiency and Renewable Energy Program, under Award Number DE-EE0006335. The lithographic printing (C.R.B. and S.Y.) was supported by the Bay Area Photovoltaics Consortium under Award Number DE-EE0004946. One of us (A.M.B.) was supported by the National Science Foundation (NSF) and the Department of Energy (DOE) under NSF CA No. EEC-1041895. S.Y. acknowledges the Kavli Nanoscience Institute and the Joint Center for Artificial Photosynthesis. The authors acknowledge Mathieu Boccard (Arizona State University) for providing the solar cells used to carry out this study. The authors thank Cristofor A. Flowers (California Institute of Technology) for helpful discussion and Lucas Meza (California Institute of Technology) for two-photon lithography advice.

Received: April 7, 2016

Revised: May 17, 2016

Published online: June 10, 2016

-
- [1] K. Masuko, M. Shigematsu, T. Hashiguchi, D. Fujishima, M. Kai, N. Yoshimura, T. Yamaguchi, Y. Ichihashi, T. Mishima, N. Matsubara, T. Yamanishi, T. Takahama, M. Taguchi, E. Maruyama, S. Okamoto, *IEEE J. Photovoltaics* **2014**, 4, 1433.
- [2] M. Taguchi, A. Yano, S. Tohoda, K. Matsuyama, Y. Nakamura, T. Nishiwaki, K. Fujita, E. Maruyama, *IEEE J. Photovoltaics* **2014**, 4, 96.
- [3] M. A. Green, K. Emery, Y. Hishikawa, W. Warta, E. D. Dunlop, *Prog. Photovoltaics: Res. Appl.* **2016**, 24, 3.
- [4] K. M. Yu, M. A. Mayer, D. T. Speaks, H. He, R. Zhao, L. Hsu, S. S. Mao, E. E. Haller, W. Walukiewicz, *J. Appl. Phys.* **2012**, 111, 123505.
- [5] M. Morales-Masis, S. M. De Nicolas, J. Holovsky, S. De Wolf, C. Ballif, *IEEE J. Photovoltaics* **2015**, 5, 1340.
- [6] L. Barraud, Z. Holman, N. Badel, P. Reiss, A. Descoedres, C. Battaglia, S. De Wolf, C. Ballif, *Sol. Energy Mater. Sol. Cells* **2013**, 115, 151.
- [7] T. Koida, H. Fujiwara, M. Kondo, *Sol. Energy Mater. Sol. Cells* **2009**, 93, 851.
- [8] E. Kobayashi, Y. Watabe, T. Yamamoto, Y. Yamada, *Sol. Energy Mater. Sol. Cells* **2016**, 149, 75.
- [9] P.-C. Hsu, S. Wang, H. Wu, V. K. Narasimhan, D. Kong, H. R. Lee, Y. Cui, *Nat. Commun.* **2013**, 4, 2522.
- [10] J. van de Groep, P. Spinelli, A. Polman, *Nano Lett.* **2012**, 12, 3138.
- [11] F. Afshinmanesh, A. G. Curto, K. M. Milaninia, N. F. van Hulst, M. L. Brongersma, *Nano Lett.* **2014**, 14, 5068.
- [12] P. G. Kik, *Opt. Lett.* **2014**, 39, 5114.
- [13] J. S. Ward, A. Duda, D. J. Friedman, J. Geisz, W. McMahon, M. Young, *Prog. Photovoltaics: Res. Appl.* **2015**, 23, 646.
- [14] S. R. Wenham, M. A. Green, US Patent, US4726850 A **1988**.
- [15] E. M. Sachs, J. Serdy, A. Gabor, F. Van Mierlo, T. Booz, in *Proc. 24th Eur. Photovoltaic Solar Energy Conf. Exhib.*, WIP, München, Germany **2009**, p. 3222.
- [16] J. Schneider, M. Turek, M. Dyrba, I. Baumann, B. Koll, T. Booz, *Prog. Photovoltaics: Res. Appl.* **2014**, 22, 830.
- [17] P. Kuang, J. M. Park, W. Leung, R. C. Mahadevapuram, K. S. Nalwa, T. G. Kim, S. Chaudhary, K.-M. Ho, K. Constant, *Adv. Mater.* **2011**, 23, 2469.
- [18] K. Ellmer, *Nat. Photonics* **2012**, 6, 809.
- [19] Q. Zheng, Z. Li, J. Yang, J.-K. Kim, *Prog. Mater. Sci.* **2014**, 64, 200.
- [20] V. K. Narasimhan, T. M. Hymel, R. A. Lai, Y. Cui, *ACS Nano* **2015**, 9, 10590.
- [21] M. F. Schumann, S. Wiesendanger, J. C. Goldschmidt, B. Bläsi, K. Bittkau, U. W. Paetzold, A. Sprafke, R. B. Wehrspohn, C. Rockstuhl, M. Wegener, *Optica* **2015**, 2, 850.
- [22] A collection of resources for the photovoltaic educator, <http://pveducation.org/pvcdrom> (accessed: September 2015).
- [23] M. W. Rowell, M. D. McGehee, *Energy Environ. Sci.* **2011**, 4, 131.
- [24] Z. C. Holman, A. Descoedres, L. Barraud, F. Z. Fernandez, J. P. Seif, S. De Wolf, C. Ballif, *IEEE J. Photovoltaics* **2012**, 2, 7.
- [25] M. A. Green, *Solar cells: operating principles, technology, and system applications*, Prentice Hall, Upper Saddle River, NJ, USA, **1982**.
- [26] M. Filipič, Z. C. Holman, F. Smole, S. De Wolf, C. Ballif, M. Topič, *J. Appl. Phys.* **2013**, 114, 074504.
- [27] S. Y. Herasimenka, W. J. Dauksher, S. G. Bowden, *Appl. Phys. Lett.* **2013**, 103, 053511.
- [28] V. E. Ferry, M. A. Verschuuren, H. B. Li, E. Verhagen, R. J. Walters, R. E. Schropp, H. A. Atwater, A. Polman, *Opt. Exp.* **2010**, 18, A237.
- [29] M. Henry, S. Walavalkar, A. Homiyk, A. Scherer, *Nanotechnology* **2009**, 20, 255305.
- [30] M. D. Henry, *PhD Thesis*, California Institute of Technology, **2010**.

ADVANCED OPTICAL MATERIALS

Supporting Information

for *Adv. Optical Mater.*, DOI: 10.1002/adom.201600252

Effectively Transparent Front Contacts for Optoelectronic
Devices

*Rebecca Saive, Aleca M. Borsuk, Hal S. Emmer, Colton R.
Bukowsky, John V. Lloyd, Sisir Yalamanchili, and Harry A.
Atwater**

Supplemental: Effectively transparent front contacts for optoelectronic devices

Rebecca Saive¹, Aleca M. Borsuk¹, Hal S. Emmer¹, Colton R. Bukowsky¹, John V. Lloyd¹, Sisir Yalamanchili¹, and Harry A. Atwater^{1*}

¹ Department of Applied Physics and Material Science, California Institute of Technology, Pasadena, CA 91125, USA

S1: Optical simulations and measurements of the wavelength and angle dependence

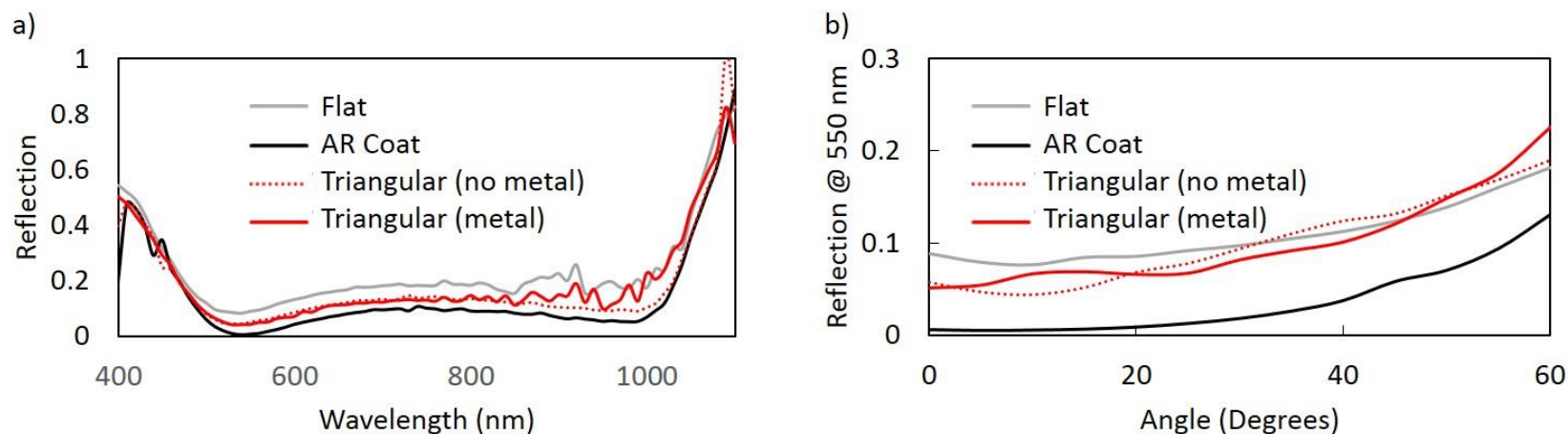


Figure S1.1: a) Measured wavelength dependent reflection and b) angle dependent reflection of areas on the solar cell with flat lines, triangular cross-section lines and only the antireflection coating. Angle and wavelength dependent reflection measurements were performed in a spectrophotometer equipped with an integrating sphere. The spectrophotometer instrument uses chopped monochromated light from a supercontinuum laser and a silicon photodiode detector, as described elsewhere (M.D. Kelzenberg, PhD thesis, 2010). The axis of angular rotation was aligned parallel to the contact finger lines or triangular contacts (compare angle α in Fig. S1.2). In contrast to the spatially resolved photocurrent measurements presented in the main manuscript in Fig. 2 the illumination spot size used in these measurements is large ($\sim 200 \mu\text{m}$), and averages over regions with good fidelity in the fabricated triangular cross-section contact structure, along with regions containing imperfections.

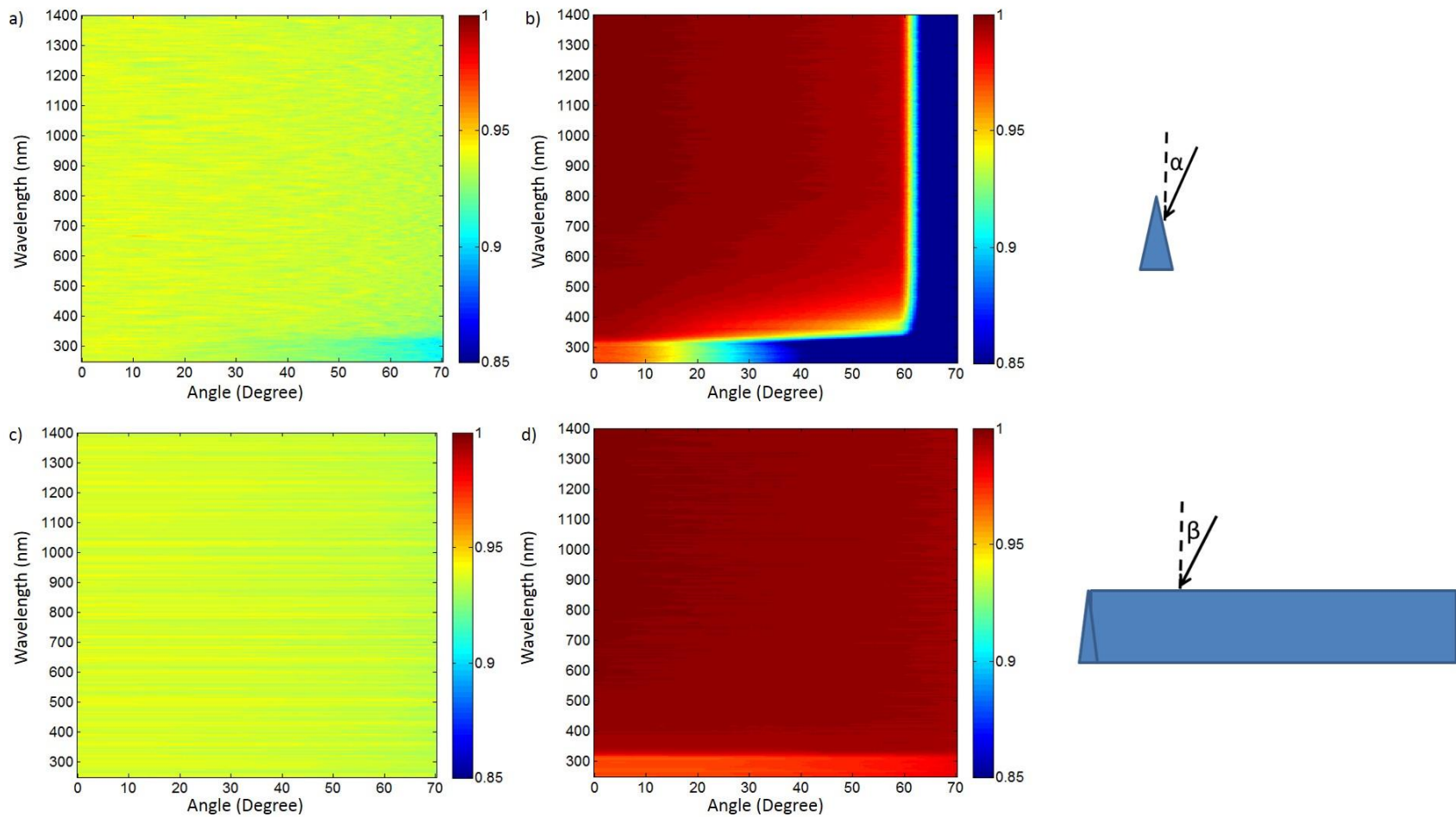


Figure S1.2: Ray optical (Lighttools) simulation of the wavelength and angle dependence of the transmission through a grid of free-standing a), c) flat silver lines and b), d) triangular cross-section silver lines. In a) and b) the angle was varied perpendicular to the line (angle α on the right side), in c) and d) the angle was varied parallel to the contact lines (angle β on the right side). Decreased transparency in the short wavelength regime can be attributed to losses in the silver.

S2 Optical simulation of triangular cross-section line patterns with different periods

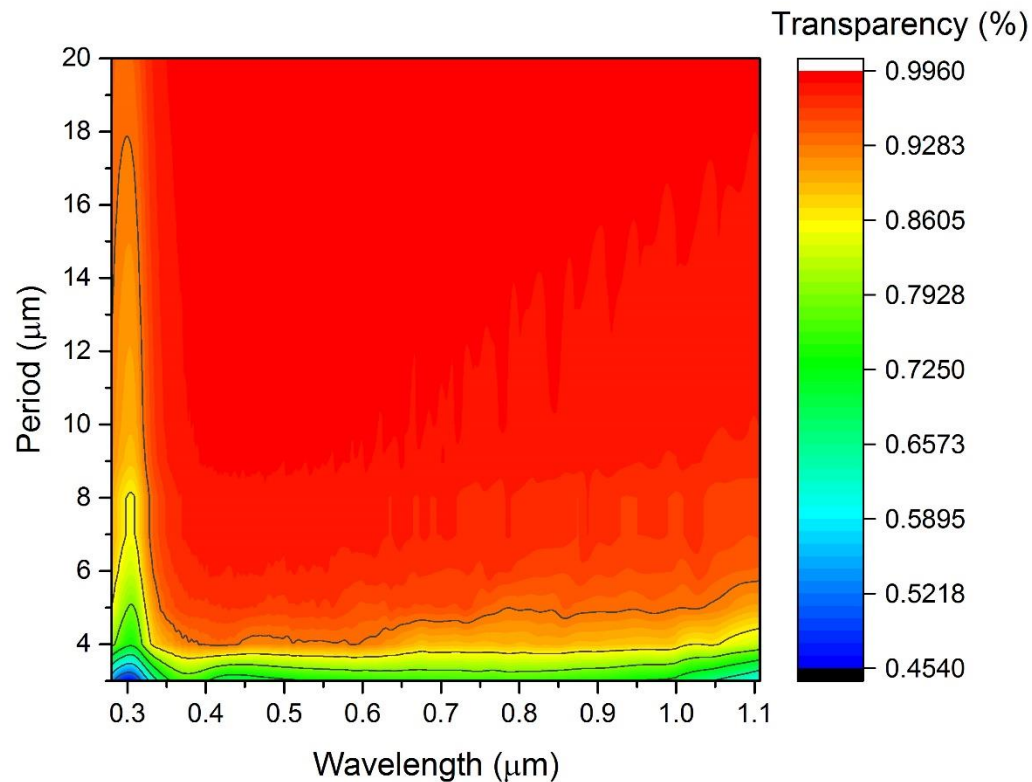
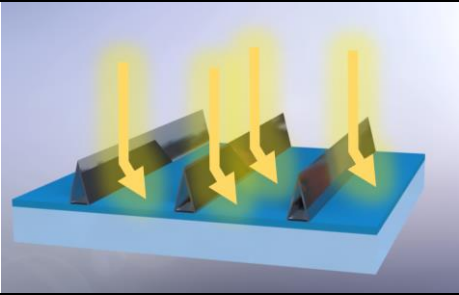
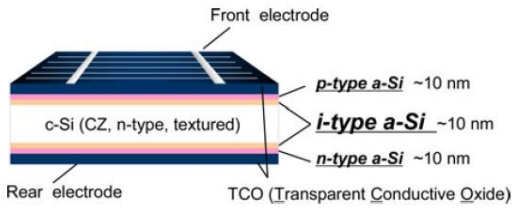
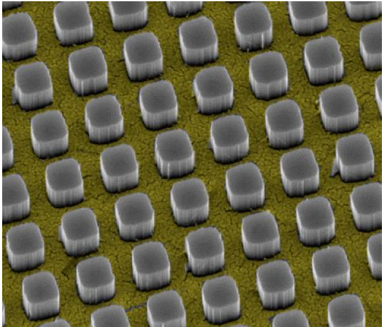
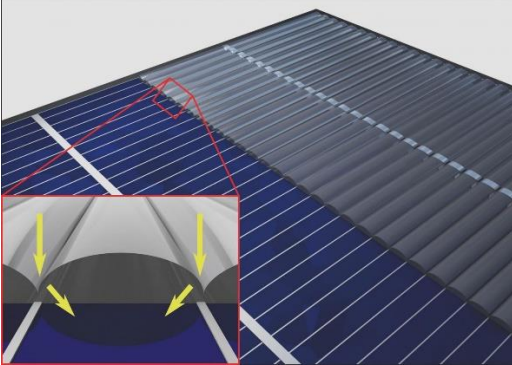
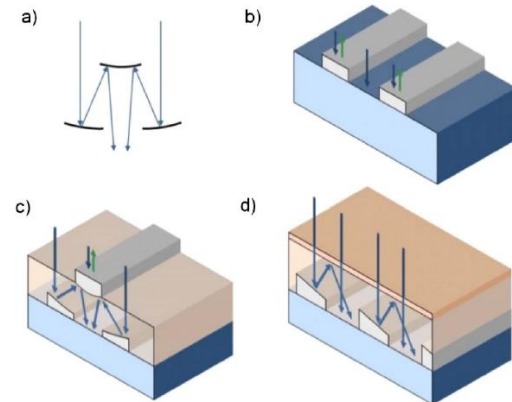
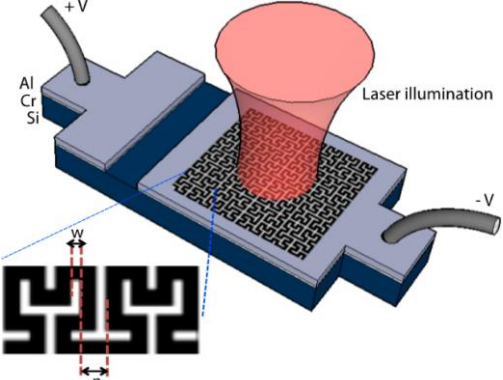
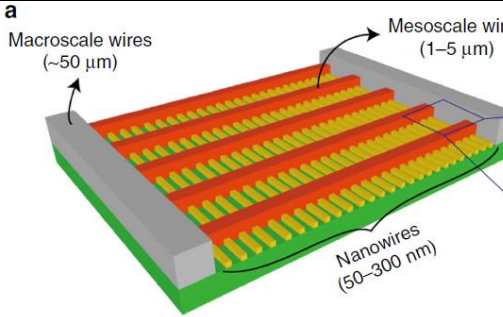
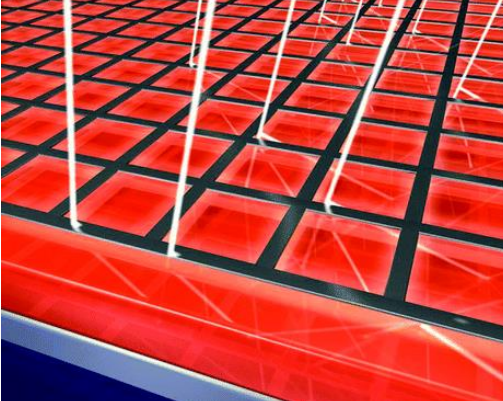


Figure S2: Simulation of the transparency of free-standing, solid silver triangular cross-section lines depending on the wavelength and on the period of the line pattern. The simulation was performed by two-dimensional rigorous coupled wave analysis (RCWA) using RSoft's DiffractMOD in order to account for wave optical effects occurring particularly for smaller periods. Periods between 3 μm and 20 μm and wavelengths between 280 nm and 1107 nm were simulated. The triangular lines were 2.5 μm wide and 7.0 μm high. Thus, e.g. a period of 6.0 μm corresponds to a gap of 3.5 μm . It can be seen that the transparency remains almost 100 % for periods down to around 5 μm . Decreased transparency in the short wavelength regime can be attributed to losses in the silver.

S3: Comparison of different photonic approaches to improved front contact transparency

Title	Authors	Paper	Scheme	Transparency	Equivalent current*	Sheet resistance
Effectively transparent front contacts for optoelectronic devices	Rebecca Saive, Aleca M. Borsuk, Hal S. Emmer, Colton R. Bukowsky, John V. Lloyd, Sisir Yalamanchili, and Harry A. Atwater	This paper		99.9 %	41.21 mA/cm ²	4.8 Ω/sq
24.7% Record Efficiency HIT Solar Cell on Thin Silicon Wafer	Mikio Taguchi, Ayumu Yano, Satoshi Tohoda, Kenta Matsuyama, Yuya Nakamura, Takeshi Nishiwaki, Kazunori Fujita, and Eiji Maruyama	IEEE Journal of Photovolt aics 4, 96-99 (2014)		~ 96.6 % ¹ (only grid fingers, deduced from geometry and current)	39.5 mA/cm ²	~ 5 Ω/sq ¹
Hybrid Metal–Semiconductor Nanostructure for Ultrahigh Optical Absorption and Low Electrical Resistance at Optoelectronic Interfaces	Vijay K. Narasimhan, Thomas M. Hymel, Ruby A. Lai, and Yi Cui	ACS nano 9, 10590-10597 (2015)		97 % absorption, with 4.2 % parasitic absorption within metal → 92.8 % transmission	38.40 mA/cm ²	Below 20 Ω/sq

<p>Cloaked contact grids on solar cells by coordinate transformations: designs and prototypes</p>	<p>Martin F. Schumann, Samuel Wiesendanger, Jan Christoph Goldschmidt, Benedikt Bläsi, Karsten Bittkau, Ulrich W. Paetzold, Alexander Sprafke, Ralf B. Wehrspohn, Carsten Rockstuhl, and Martin Wegener</p>	<p><i>Optica</i> 2, 850-853 (2015)</p>		<p>Transparency not explicitly reported.</p>	<p>---</p>	<p>Not reported but this geometry should allow for low sheet resistance.</p>
<p>Catoptric electrodes: transparent metal electrodes using shaped surfaces</p>	<p>Pieter G. Kik</p>	<p><i>Optics letters</i> 39, 5114-5117 (2014)</p>		<p>84 % (Simulation)</p>	<p>34.68 mA/cm²</p>	<p>Not reported but this geometry should allow for low sheet resistance.</p>

<p>Transparent metallic fractal electrodes for semiconductor devices</p>	<p>Farzaneh Afshinmanesh, Alberto G. Curto, Kaveh M. Milaninia, Niek F. van Hulst, and Mark L. Brongersma</p>	<p><i>Nano letters</i> 14, 5068-5074 (2014)</p>		<p>No average transparency reported.</p>	<p>---</p>	<p>No sheet resistance reported.</p>
<p>Performance enhancement of metal nanowire transparent conducting electrodes by mesoscale metal wires</p>	<p>Po-Chun Hsu, Shuang Wang, Hui Wu, Vijay K. Narasimhan, Desheng Kong Hye Ryoung Lee and Yi Cui</p>	<p><i>Nature communications</i> 4 (2013)</p>		<p>92 %</p>	<p>38.10 mA/cm²</p>	<p>0.36 Ω/sq</p>
<p>Transparent Conducting Silver Nanowire Networks</p>	<p>Jorik van de Groep, Pierpaolo Spinelli, and Albert Polman</p>	<p><i>Nano Letters</i> 12, 3138-3144 (2012)</p>		<p>91 %</p>	<p>37.67 mA/cm²</p>	<p>6.5 Ω/sq</p>

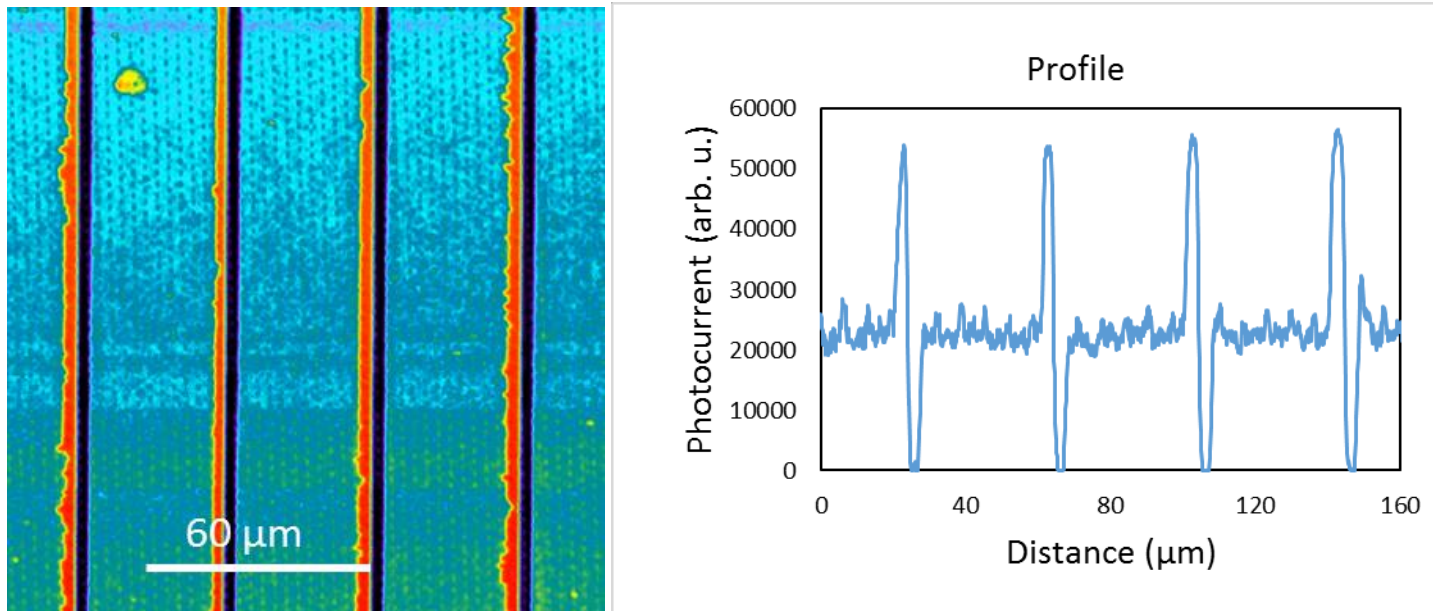
* The equivalent circuit is calculated at the example of the 24.7 % efficiency Panasonic HIT cell (*IEEE Journal of Photovoltaics* **4**, 96-99 (2014)). The grid fingers are replaced by using a contact structure with the reported transparency, the busbars are kept the same. Furthermore, a current of 1.21 mA/cm^2 is subtracted in order to account for parasitic absorption within the amorphous silicon.

For our contact structure we also performed a realistic ray tracing simulation that takes the front texture of silicon in real solar cells and losses in the amorphous silicon into account. Note, that it is not clear for all structures reported here how integration with structured silicon would be achieved.

¹ These values are not explicitly given in the paper but deduced from the optical and electrical properties by comparison with similar solar cells.

S4: Additional spatially resolved laser beam induced photocurrent measurement

The left figure shows a spatially resolved laser beam induced photocurrent measurement of an area on the very same solar cell used for the measurement in Fig 2. In this area an approximately 100 nm silver layer covers the flat lines as a result from the angular evaporation. The silver was evaporated from the right side so that right of the line there is a silver hill while left of the line is only little or no silver. From the profile shown on the right side, it can be seen that there is a non-negligible photocurrent induced between the lines although this area was covered with around 100 nm of silver. The signal goes down to zero at the position of the silver hills showing that this is not a measurement artifact but that 100 nm of silver transmit a significant amount of light.



S5: Electrical properties of the line grid

$$P_{loss} = I^2 R = \underbrace{\frac{1}{2} \int_0^{w/2} j^2(x, y) x^2 L^2 \rho_{\square} \frac{dx}{L}}_{\text{Charge generation profile}} + \underbrace{\int_0^L j^2(x, y) w^2 y^2 \rho_{Ag} \frac{dy}{t_{Ag} w_{Ag}}}_{\text{Transport within metal finger}}$$

$$\rightarrow P_{loss} = j^2 L \rho_{\square} \frac{w^3}{24} + j^2 w^2 \rho_{Ag} \frac{L^3}{3 t_{Ag} w_{Ag}} = I^2 \rho_{\square} \frac{w}{24L} + I^2 \rho_{Ag} \frac{L}{3 t_{Ag} w_{Ag}}$$

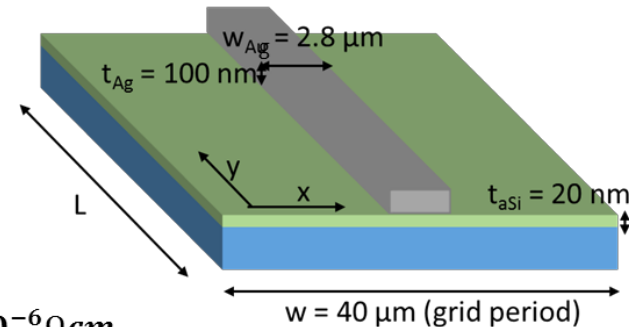
(with $j^2(x, y) = \text{const}$)

Assuming a length of 1 cm with the device geometry shown we obtain:

$$R_s = P_{loss} / I^2 = 1.0 \Omega \text{cm}^2$$

with $\rho_{\square(a-si)} = 400 \text{ k}\Omega/\text{sq}^*$ and $\rho_{Ag} = 1.6 \cdot 10^{-6} \Omega \text{cm}$.

(With $j = 40 \text{ mA/cm}^2$ the power loss would amount to 1.6 mW/cm^2)



*Filipic et al.: JOURNAL OF APPLIED PHYSICS 114, 074504 (2013)